



JGR Space Physics

RESEARCH ARTICLE

10.1029/2021JA029340

Key Points:

- Increasing subauroral polarization streams (SAPS) velocity expands longitudinally from post-dusk side in main phase and shrinks back to post-dusk side in recovery phase
- In the main phase, SAPS T-Slope has similar time profile with SYMH index and ring current strongly controls the velocity evolution
- Good linear correlations exist between SAPS velocity and SYMH/ AE/Bz while the correlations are different in different phases

Correspondence to:

Y. C.-M. Liu, liuyong@swl.ac.cn

Citation:

Zhang, Q., Liu, Y. C.-M., Zhang, Q.-H., Xing, Z.-Y., & Ma, Y.-Z. (2021). Longitudinal evolution of the velocity of subauroral polarization streams (SAPS) in different phases of magnetic storms: SuperDARN observations. *Journal of Geophysical Research: Space Physics, 126*, e2021JA029340. https://doi.org/10.1029/2021JA029340

Received 30 MAY 2021 Accepted 14 AUG 2021

Longitudinal Evolution of the Velocity of Subauroral Polarization Streams (SAPS) in Different Phases of Magnetic Storms: SuperDARN Observations

Qiang Zhang^{1,2}, Yong C.-M. Liu¹, Q.-H. Zhang³, Zan-Yang Xing³, and Yu-Zhang Ma³

¹State Key Laboratory of Space Weather, National Space Science Center, CAS, Beijing, China, ²University of Chinese Academy of Sciences, Beijing, China, ³Shandong Provincial Key Laboratory of Optical Astronomy and Solar-Terrestrial Environment, Shandong University, Institute of Space Sciences, Weihai, China

Abstract Investigations of the evolution of subauroral polarization streams (SAPS) are important to understand the plasma transport processes in the polar ionosphere. In this article, three cases of SAPS evolution are analyzed using the observations made by the Super Dual Auroral Radar Network mid-latitude radar chain, Special Sensor Ultraviolet Spectrographic Imagers instrument and Active Magnetosphere and Planetary Electrodynamics Response Experiment. The three cases occur in the main phase, beginning of recovery phase and end of recovery phase of three magnetic storms. The cases last from 1.5 to 2 h during 1800–0300 MLT (magnetic local time). The observations show that the SAPS velocity evolution is strongly controlled by the ring current injection during the storm main phase. The responses of SAPS velocity are prompt and appear first near the dusk side and then expand to the night side. Besides, the SAPS velocity has a good linear correlation (R = -0.85) with SYMH index during the evolution of the magnetic storm. The SAPS velocity also shows dependence on the AE index and interplanetary magnetic field (IMF) Bz. The correlations between SAPS velocity and AE/Bz increase with the decay of the magnetic storm. However, the effect of substorm/IMF on SAPS velocity is not strong compared to that of the magnetic storm.

1. Introduction

Large and strong ions flow (>100 m/s), named as subauroral polarization streams (SAPS), mainly happen in the terrestrial ionosphere dusk-night side and subauroral region during geomagnetic storms and substorms (Anderson et al., 1991, 1993; Foster & Vo, 2002; Galperin et al., 1974; Karlsson et al., 1998; Spiro et al., 1979). SAPS consist parts of subauroral ion drifts (SAID) and westward flows in broader subauroral regions (Yeh et al., 1991). SAID is the localized westward ion flow at speed more than 1 km s⁻¹ with a latitudinal width of 1°-2° (Anderson et al., 1993, 2001; He et al., 2014; Karlsson et al., 1998). Convention cells are known to form in the polar ionosphere through the magnetosphere-ionosphere coupling processes (Dungey, 1961; Zhang et al., 2013, 2015). A series of plasma irregularities generate in development including storm-enhanced density, tongue of ionosphere, polar cap patches, ionospheric trough, and SAPS (e.g., Foster & Burke, 2002; Foster et al., 2004, 2005; Zhang et al., 2011, 2013). It is believed that SAPS form with the force of the polarization drifts after the R2 field-aligned currents (FACs) flowing into the low-conductance ionospheric region such as the ionospheric trough. The ions flow in the SAPS channel can get thousand meters per second velocity values (Anderson et al., 1993, 2001; Schunk et al., 1976). Several statistical studies and case studies using satellites and radars show the characteristics of SAPS. SAPS appear on the equatorward side of the auroral oval boundary, sometimes locate at the boundary. With the enhancement of geomagnetic disturbance, SAPS become strong and rapid and extend to lower latitudes, which can also induce the ions upflow similar to that of other irregularities because of the frictional heating and other factors (e.g., Buonsanto et al., 1992; Erickson et al., 2010; Heelis et al., 1993; Ma et al., 2018; Wang & Lühr, 2013; Yeh & Foster, 1990; Yuan et al., 2008; Zhang et al., 2016, 2020; Q.-H. Zhang et al., 2017; S.-R. Zhang et al., 2017; Zou et al., 2017). SAPS cover the post-noon side, dusk side, and midnight side, from about 1400 to 0300 MLT. From the night side to the noon side, SAPS velocity becomes rapid and SAPS gradually merge with the sunward return flows into the afternoon convection cells. In the longitude coverage of SAPS, most SAPS events occur between 1800 and 2100 MLT. Several magnetic factors are also found to be related to SAPS such as Kp, Dst, IMF, cross polar cap potential, conductance, electrojet, and zonal wind as shown in many reports (e.g., Aa

© 2021. American Geophysical Union. All Rights Reserved.

ZHANG ET AL. 1 of 16



et al., 2020; Foster & Vo, 2002; Huang & Foster, 2007; Kunduri et al., 2017; Wang et al., 2008, 2011; Zheng et al., 2008). Besides, SAPS are divided into several types because of the morphological features, such as double subauroral ion drifts (DSAID) and abnormal subauroral ion drifts/abnormal subauroral polarization drifts that are different in their formation mechanisms (Ebihara et al., 2008; He et al., 2014, 2016; Horvath & Lovell, 2017, 2018; Liléo et al., 2010; Voiculescu & Roth, 2008).

Because of the limitation of the observation techniques, a few direct observations of SAPS evolution have been reported. Some studies have focused on the main phase of the big storms. Oksavik et al. (2006) present the first observation of one SAPS channel using SuperDARN Wallops high-frequency (HF) radar. They observe the event over large distances (~hundreds of km) and extended time intervals (~hours). The observation is from 2200 to 0200 MLT and shows the equatorward latitude movement of the SAPS velocity peak. They propose that some variations of SAPS may be induced by the IMF factors. The observation shows only part of the whole evolution process because of the limitation of the single radar coverage. The observation tracks the partial SAPS evolution integrally and demonstrates the practicability of the Wallops HF radar. Clausen et al. (2012) observe the large-scale SAPS longitudinal velocity variations using six mid-latitude SuperDARN radars. The observation covers the midnight sector and part of the morning sector from 2300 to 0600 MLT during the main phase of a magnetic storm for 6 h which is the large-scale observation for the first time. The flows within the SAPS are predominantly westward. The SAPS velocity magnitude decreases with the MLT in the morning sector which is similar to previous studies (e.g., Erickson et al., 2011; Foster & Vo, 2002; Kunduri et al., 2017, 2018; Zhang et al., 2020). By model simulation, they propose that the pressure distribution in the magnetospheric equatorial plane probably partly determines the ionospheric velocities. He et al. (2017) also present the different evolution patterns of SAPS during the magnetic storm and quiet time substorms using the Defense Meteorological Satellite Program (DMSP). In their study, the southward IMFs show important effects to the lifetime of SAPS. The relation between SAPS and IMF is very close. In the next year, they present the observation of the large-scale structures of SAPS also by DMSP satellites during a major magnetic storm (He et al., 2018). The observations by the four DMSP satellites cover most regions of the SAPS, which can partly show the SAPS evolution. The SAPS are highly dynamic during storms and are observed first in the dusk side at initial phase; then expand toward the midnight sector and move to lower latitudes as the main phase progressed. They also propose that there is a close relationship between SAPS and IMF. Because of the lack of continuous cover of the satellites, the evolution of SAPS is presented fragmentarily while they also present meaningful information in ingenious ways. Besides, they report the first observation of the SAPS oscillations in the process of the SAPS evolution (He et al., 2019). The strong effects of the IMF on the inner magnetosphere-ionosphere coupling are also presented. Besides, some studies present the SAPS evolution during recovery phase of the storms. Wang et al. (2019) present a case study of the dynamic temporal evolution of SAPS near the Harang reversal during a storm recovery phase using conjugate observations by the Van Allen Probes and the SuperDARN radars. In their study, the mesoscale enhancement of SAPS is associated with energetic ion flux increase, energetic electron flux decrease and local magnetic field dip. They suggest that SAPS can be generated directly due to the particle injections. Horvath and Lovell (2021) present several scenarios depicting the development of various types (SAPS, structured SAPS and DSAID) of large subauroral flows (~3,000 m s⁻¹) during the initial phase and recovery phase of a super storm using multi-instrument measurements (Cluster, Los Alamos National Laboratory, DMSP and Challenging Minisatellite Payload). The large-scale TIDs (Traveling Ionospheric Disturbances) develop deepened the trough and enhance the SAPS via positive feedback mechanisms. They propose that the strong M-I-T coupling plays an important role in the enhancement of SAPS.

In general, the direct observations of SAPS evolution have been presented during the main phase and recovery phase of the big storms through a series of case studies and the effects of the magnetic storm, substorm and IMF have been revealed. Nevertheless, the related process also needs more detailed studies and observations. For example, what are the characteristics and differences of the SAPS velocity during SAPS evolution in different magnetic storm phases? Besides, the relations between SAPS and magnetic storm, substorm, and IMFs in different phases also need further investigation. In our study, the mentioned relations are mainly exhibited through the correlation analysis between SAPS velocity and geomagnetic indices (SYMH, AE, and IMF Bz). Although a number of statistical correlation studies between SAPS and these geomagnetic indices are reported (e.g., Aa et al., 2020; Erickson et al., 2011; Foster & Vo, 2002; Huang & Foster, 2007; Kunduri et al., 2017; Wang et al., 2008), the direct correlation analyses between SAPS velocity

ZHANG ET AL. 2 of 16

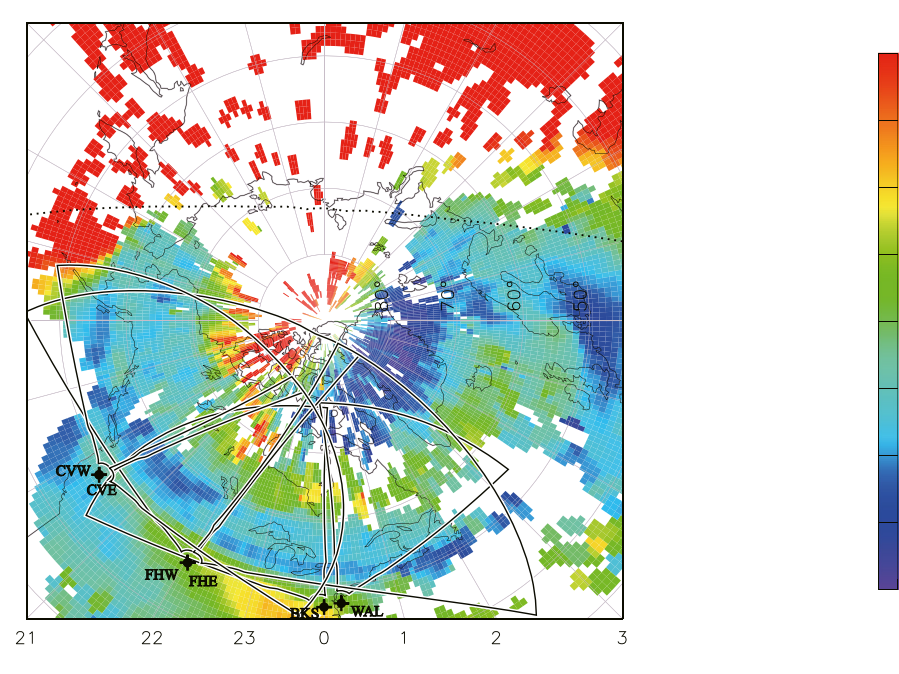


Figure 1. The position and coverage of the SuperDARN midlatitude six-radar chain (CVW, CVE, FHW, FHE, BKS, and WAL) and the total electrons content (TEC) distribution in 0505–0510 UT on February 19, 2014. The black star points represent the radar positions. The fan planes show the coverage of the six radars. The colorbar shows the TEC ranging 0–20 TECU. The gridding shows the MLAT-MLT coordinates (MLAT: from 40° to 90°). The dotted line shows the day/night terminator.

and SYMH/AE/Bz in specific cases are also needed. The structure of our article is divided as following: In Part 2, we introduce the instruments used and method of analysis and in Part 3, we present the observations of SAPS evolutions in different magnetic storm phases. The detailed discussions of the correlations between SAPS velocity and relevant geomagnetic indices in specific cases are presented in Part 4.

2. Data Sets

2.1. SuperDARN Radars

Super Dual Auroral Radar Network is an international radar network for studying the variations of the plasma in the upper atmosphere and the ionosphere. The radar network contains more than 30 HF radars in both northern and southern hemispheres. The coverage of the radars ranges from mid-latitude to polar region. The radars are capable of operating in the high-frequency band between 8 and 18 MHz (Chisham et al., 2007; Greenwald et al., 1995). The radars are generally used to measure the Doppler velocity of plasma in the ionosphere and other effects. Operating in the standard mode, the radars have several observation directions called beams. The beam covers the azimuth about 3° and the total scanning time is about 1 min; and the number of radar beams is different for different radars. Besides, each beam is divided into 75 range gates of length 45 km. The radars provide data by receiving the backscatter echoes reflecting from the plasma density irregularities that generally existed in the F region of the ionosphere. SuperDARN radars are the most effective way to observe the evolution of large-scale SAPS. In our study, we use the data of the six mid-latitude radars containing Christmas Valley East, Christmas Valley West, Fort Hays East, Fort Hays West, Blackstone, and Wallops Island (CVE, CVW, FHE, FHW, BKS, and WAL).

Figure 1 shows the coverage and position of the six-radar chain in magnetic latitude (MLAT)-MLT coordinates on February 19, 2014, 0505–0510 UT. The colorbar shows the total electrons content (TEC), ranging

ZHANG ET AL. 3 of 16



 $1-20~\rm TECU~(1~\rm TECU=10^{16}~el~m^{-2})$. The dotted lines show the day/night terminator. The fan-shaped solid lines show the field of view of each radar. Figure 1 is drawn using the online plotting tool available at http://vt.superdarn.org/tiki-index.php. The six-radar chain observes all of the dusk and midnight regions (approximately from 1800 to 0200 MLT) where the SAPS are observed frequently. Besides, continuous and narrow ionosphere trough is observed around 62° which is often accompanied by SAPS; the TEC within the trough drops to $4-7~\rm TECU$ while that in the vicinity is larger than $10~\rm TECU$.

2.2. SSUSI Instrument and AMPERE

Special Sensor Ultraviolet Spectrographic Imagers are remote sensing instruments carried by DMSP. The SSUSI comprise an Ultraviolet Spectrographic Imaging System and a Nadir-looking Photometer System. The measurement range of SSUSI is from the extreme ultraviolet to the far ultraviolet and the wavelength range is from 80 to 170 nm. The resolution is 1.8 nm (Morrison et al., 2002; Paxton et al., 2002). SSUSI provide important information in the monitoring ionosphere and thermosphere such as the auroral oval imaging, precipitating electron energy flux and densities in F-region ionosphere, and neutral composition in dayside. In our study, the auroral emissions and empirical models provided by SSUSI data are used to identify the equatorward boundary of auroral oval which further determines the SAPS regions.

Besides, the Active Magnetosphere and Planetary Electrodynamics Response Experiment provides the globe FACs map which is convenient to search the dynamics of SAPS. The AMPERE magnetic perturbation data and data products are derived from Iridium engineering magnetometers, provided by the AMPERE Science Data Center (Anderson et al., 2000; Waters et al., 2001) and is available at http://ampere.jhuapl.edu/rBrowse/index.html.

2.3. Preprocessing

The directions of the velocity in SuperDARN data are lines of sight directions: away/toward the radars. The observed velocities are the components of the real flows' velocities. Several methods could be used to estimate the true direction of the flows. One is combining the data from more than two radars at the same locations thus deducing the real flow directions (Hanuise et al., 1993). The velocity we deduced here is called merged velocity. Clausen et al. (2012) provide an ingenious method to estimate the true directions which is similar to L-shell fitting (Ruohoniemi et al., 1989; Villain et al., 1987). The method needs specific data in the east-west radars to find the 0 m s⁻¹ position, then infers the real directions. In our study, we have used the method by Hanuise et al. (1993). However, there is problem that we cannot get the true velocity in the location detected by only one single radar. Because of the narrow and rapid features of SAPS, it is acceptable to assume that the directions of the nearby flows are approximately consistent, thus the true velocities in one radar detected locations share the same directions with the adjacent merged velocities. Furthermore, the true velocities in the single radar detected locations can be calculated according the determinate directions and they are called inferred velocities. Besides, the auroral map and empirical model provided by SSUSI determine the equatorward boundary of auroral oval. SAPS flows are very close to the sunward return flows in the auroral oval that both of them have similar directions, therefore, the equatorward boundary of auroral oval can also ensure the accuracy of the calculated velocity directions. In our study, for getting enough data, the spatial resolution of velocity data is 1 MLAT/0.2 MLT and temporal resolution is 4 min.

Figure 2 shows the distribution of the velocity unit vectors in MLAT-MLT coordinates on February 19, 2014, at 0508–0512 UT. The red arrows show the merged velocity unit vectors. The blue arrows show the inferred velocity unit vectors (because of the huge span of the magnitude of SAPS velocity, the figure performs poor if we consider that the lengths of the vectors represent the velocity values). The inferred velocity directions are consistent with the directions of nearby merged velocity vectors and the equatorward boundary of the auroral oval in Figure 2. The orange solid curves represent the boundary of auroral oval by the auroral oval model. The remaining colored regions show the SSUSI auroral oval map. The colorbar shows the LBHS (N_2 LBHS (N_2

ZHANG ET AL. 4 of 16

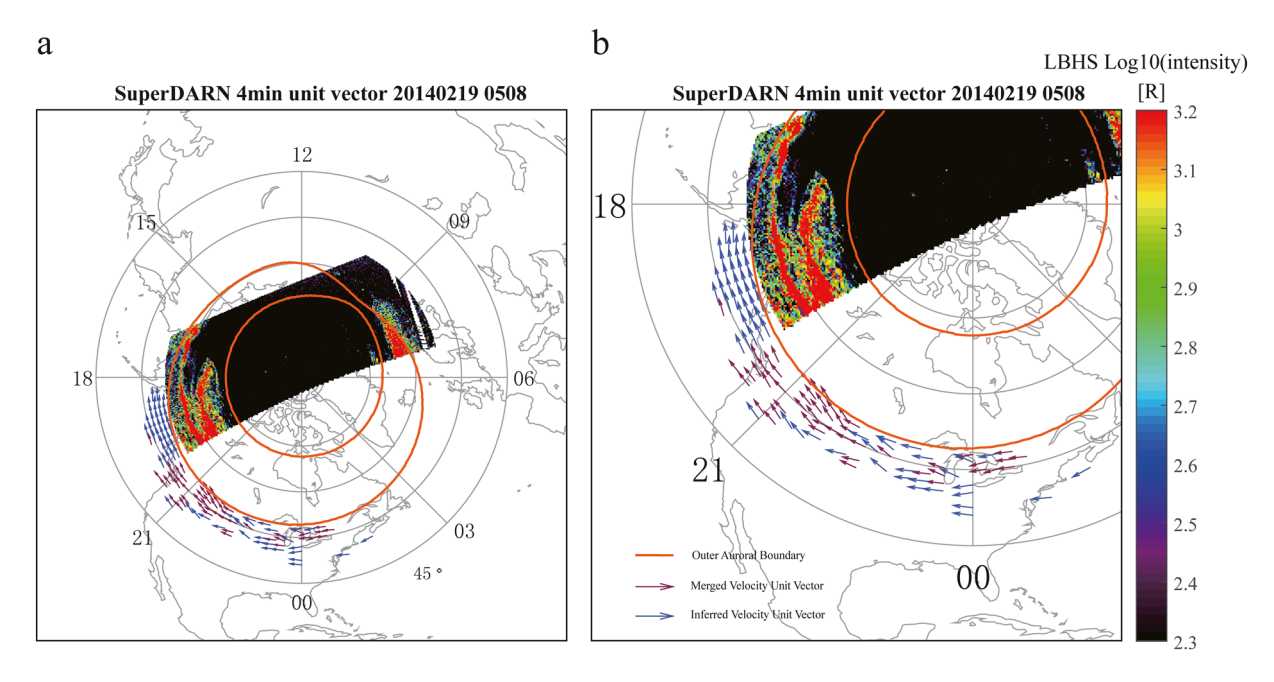


Figure 2. The distribution of the SAPS velocity unit vectors in MLAT-MLT coordinates which is converted by altitude adjustment corrected geomagnetic coordinates (AACGM) in 0508–0512 UT on February 19, 2014. The resolution is 1 MLAT/0.2 MLT. The red arrows show the merged velocity unit vectors. The blue arrows show the inferred velocity unit vectors. The orange solid curves show the modeled boundary of the auroral oval. Other colored regions show the intensity of auroral oval map provided by SSUSI instruments. The colorbar shows the LBHS. (a) The globe observations. (b) The local observations.

the polar cap region. The identification of the eastward velocity vectors ensures the longitudinal boundary of SAPS region. Besides, all SAPS velocities are valuing by the 100 m s $^{-1}$ limitation. The SAPS velocity distribution in this time segment covers the 1800–0100 MLT region. The directions of the SAPS velocity vectors are obviously westward and approximately consistent with the auroral sunward return flows directions. The equatorward boundary of auroral oval is located at $\sim\!61^\circ$ magnetic latitude in dusk side while it is $\sim\!58^\circ$ in post-dusk side. All of the vectors distribute in the equatorward region of the outer auroral boundary. Figure 2a shows the global observations and Figure 2b shows the local observations.

2.4. Observations of the Evolution of SAPS

Based on the preprocessing of radar's data in Part 2, now we present the observations. The solar wind conditions of the three observation cases are shown in Figures 3a, 4a and 5a. The three cases happen on February 19, 2014, October 25, 2011 and June 28–30, 2013, respectively. The panels from top to bottom are: (a) components of magnetic fields (Bx, By, and Bz), (b) solar wind velocity, (c) solar wind proton density, (d) solar wind dynamic pressure, (e) AE, AU, AL indices and (f) SYMH index. The shading area marks the observation period in each case. Figures 3b, 4b and 5b show the SAPS velocity distribution in MLT-UT grids for each case. We can find that in each case the observations last only for 1.5-2 h because of the limitations of the six-radar chain. Satisfyingly, the six-radar chain always focuses on the dusk-midnight region during the period where we are mostly interested. Besides, Figures 3c, 4c and 5c show the FACs distribution in MLAT-MLT coordinates for each case. The black circles are the auroral oval boundaries derived from empirical model. The range of currents is between -1 and $1~\mu A$ m⁻². The time interval between adjacent panels is chosen as 20~min. The three cases are divided according to the different magnetic storm phases. The three cases are not observed in the same magnetic storm. It is difficult to observe the all phases of the same magnetic storm event, moreover the observations need to focus on the dusk-midnight region and ensure enough data in all phases, we can find valuable features of SAPS in such highly variable magnetic activity conditions.

In the February 19, 2014 case, our interested period is marked by the shading area from 0400 to 0530 UT in Figure 3a. IMF Bz is strongly negative (\sim -15 nT) from February 18 to February 19. The intense magnetic storm starts at 1400 UT on February 18 and maintains at \sim -50 nT from 0000 to 0340 UT on February

ZHANG ET AL. 5 of 16

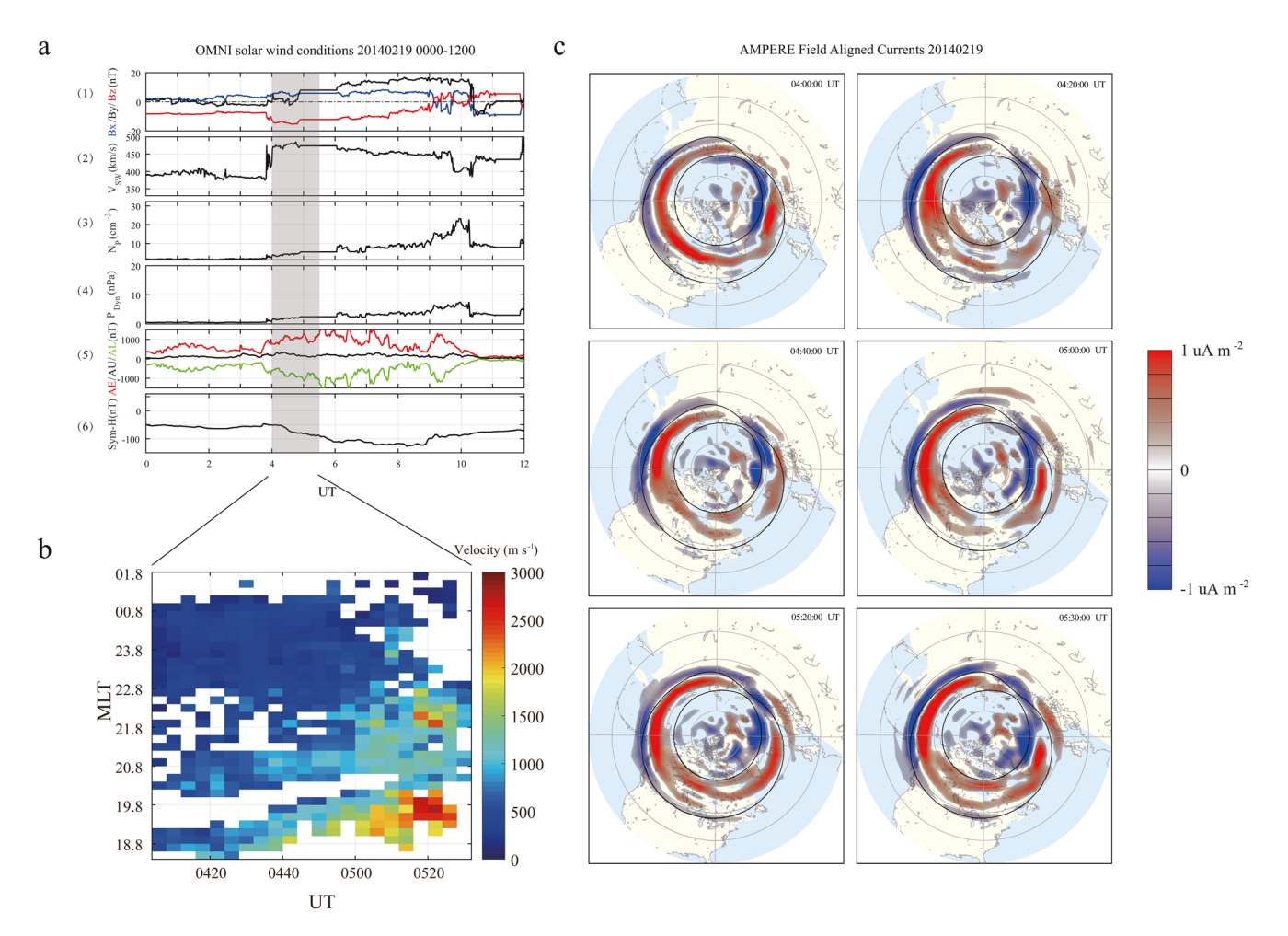


Figure 3. The solar wind conditions and corresponding subauroral polarization streams (SAPS) velocity distributions for the three cases. (a) The OMNI solar wind conditions on February 19, 2014 (1) Components of magnetic fields (Bx, By, and Bz), (2) Solar wind velocity, (3) Solar wind proton density, (4) Solar wind dynamic pressure, (5) AE, AU, AL indices and (6) SYMH index. The shaded area shows the period of interest. (b) The SAPS velocity distributions in the MLT/ UT grids of the three cases. The *x* axis represents the UT and the *y* axis represents the MLT. The colorbar shows the velocity. (c) The FACs distribution in MLAT-MLT coordinates derived from AMPERE. The black circles are the auroral oval boundaries derived from the empirical model. The range of currents is between -1 and 1 μA m⁻². The time interval between adjacent panels is chosen as 20 min.

19. From 0340 UT on February 19, the magnetic storm enhances and is accompanied by a series of large substorms with AE index increasing to about 1,000 nT. The enhanced main phase lasts from 0430 to 0830 UT. The magnetic storm lasts for several hours until the next day and the minimum SYMH index reaches -125 nT at about 0830 UT, meanwhile a series of substorms fade away after 1030 UT. On February 19, the six-radar chain records the large-scale SAPS during the intense storm in dusk-midnight region. Figure 3b shows the velocity distributions along with the MLT/UT from 0400 to 0530 UT in the February 19, 2014 case. The x axis represents the UT (0400-0530 UT) and the y axis represents the MLT (1824-0148 MLT). The colorbar shows the velocity (0-3,000 m s⁻¹). From 0400 to 0530 UT, the total velocity considering all MLTs rapidly increases with UT. The increases of SAPS velocity appear after ~0420 UT and start near the dusk side (\sim 1824–2000 MLT). After \sim 0500 UT, the velocity increases strongly and reaches to \sim 3,000 m s⁻¹ at 0520 UT. Meanwhile, the increasing velocity expands to 2248 MLT with ~2,000 m s⁻¹. Overall, the increases of SAPS velocity appear around the dusk side then expand to pre-night side in this case. The rapid increases appear at \sim 1900–2000 MLT. Besides, the velocity around midnight side maintains at \sim 500 m s⁻¹. The magnetic storm and the substorm respectively locate in the main phase and growth phase, in which period, the corresponding SYMH and AE indices also increase enormously. The result reveals that SAPS velocity evolution has similar variations with the SYMH and AE indices. Figure 3c shows the FACs during 0400-0530 UT. At the beginning, the R2 FACs appear around the outer auroral oval boundary. The R2 FACs

ZHANG ET AL. 6 of 16

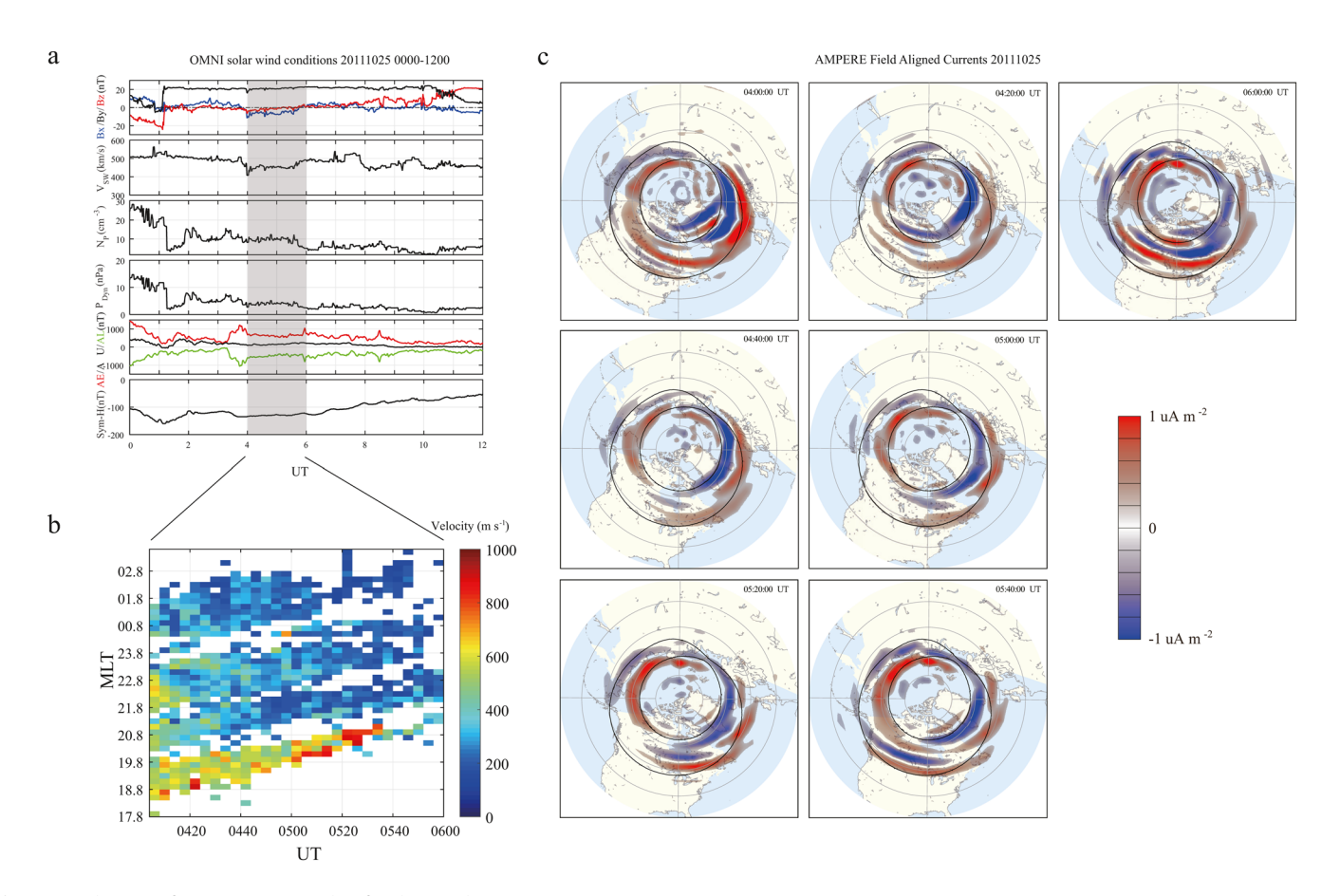


Figure 4. The same format as Figure 3 but for the October 25, 2011 case.

expand to subauroral regions around dusk side at 0420 UT when the SAPS velocity starts to increase in Figure 3b. From 0440 UT, the R2 FACs expand to \sim 1900–2000 MLT region where the SAPS velocity increases intensely. The expanded R2 FACs in subauroral region seem to correspond well with the increasing SAPS velocity embodied in temporal variation and spatial distribution. The strong azimuthal pressure gradients of the ring currents that generate the expanded R2 FACs may be the main reason for the similar variations. The result indicates that the ring currents during the main phase of the storm strongly control the SAPS velocity evolution.

Figure 4a shows the solar wind conditions on October 25, 2011. Our interested period corresponds to the part of the recovery phase of a large magnetic storm, starting at 1900 UT on October 24, reaching the lowest SYMH index of -160 nT around 0200 UT on October 25. The AE index in that region is about 600 nT, and the IMF Bz changes from -5 to 0 nT. Figure 4b shows the velocity distributions on that day with the same format as in Figure 3b. From 0400 to 0600 UT, the total velocity considering all of MLTs decreases with UT though there is a slight increase around 0530 UT with ~800 m s⁻¹. Around 0400 UT, the velocity with \sim 500–600 m s⁻¹ distributes the dusk-midnight region. After 0430 UT, the velocity (\sim 500–600 m s⁻¹) starts to shrink to dusk side. The velocity in other regions except dusk side decreases to $\sim 200-400 \text{ m s}^{-1}$. After 0500 UT, the large velocity locates on ~2000–2100 MLT. Overall, the relative large velocity regions (~500–600 m s⁻¹) shrink to dusk side from dusk-midnight region and the total velocity decreases with UT. The SAPS velocity variations correspond to the recovery phase of magnetic storms. The behavior of the SAPS velocity is also similar with the SYMH index. Besides, the variation of SAPS velocity is entirely opposite in comparison to that of the February 19, 2014 case. Figure 4c shows the FACs map on October 25, 2011. During the whole observation, the R2 FACs seem to locate in the auroral oval. Only a few R2 FACs expand to the subauroral region around dusk side. We also notice that in the 1900-2100 MLT region where the SAPS velocity maintains at ~600 m s⁻¹ has no R2 FACs distribution. Until 0540 UT, the FACs appear in that region. The R2 FACs may be weak before 0540 UT (the model data is not so clear). Unfortunately, the DMSP F16-F18

ZHANG ET AL. 7 of 16

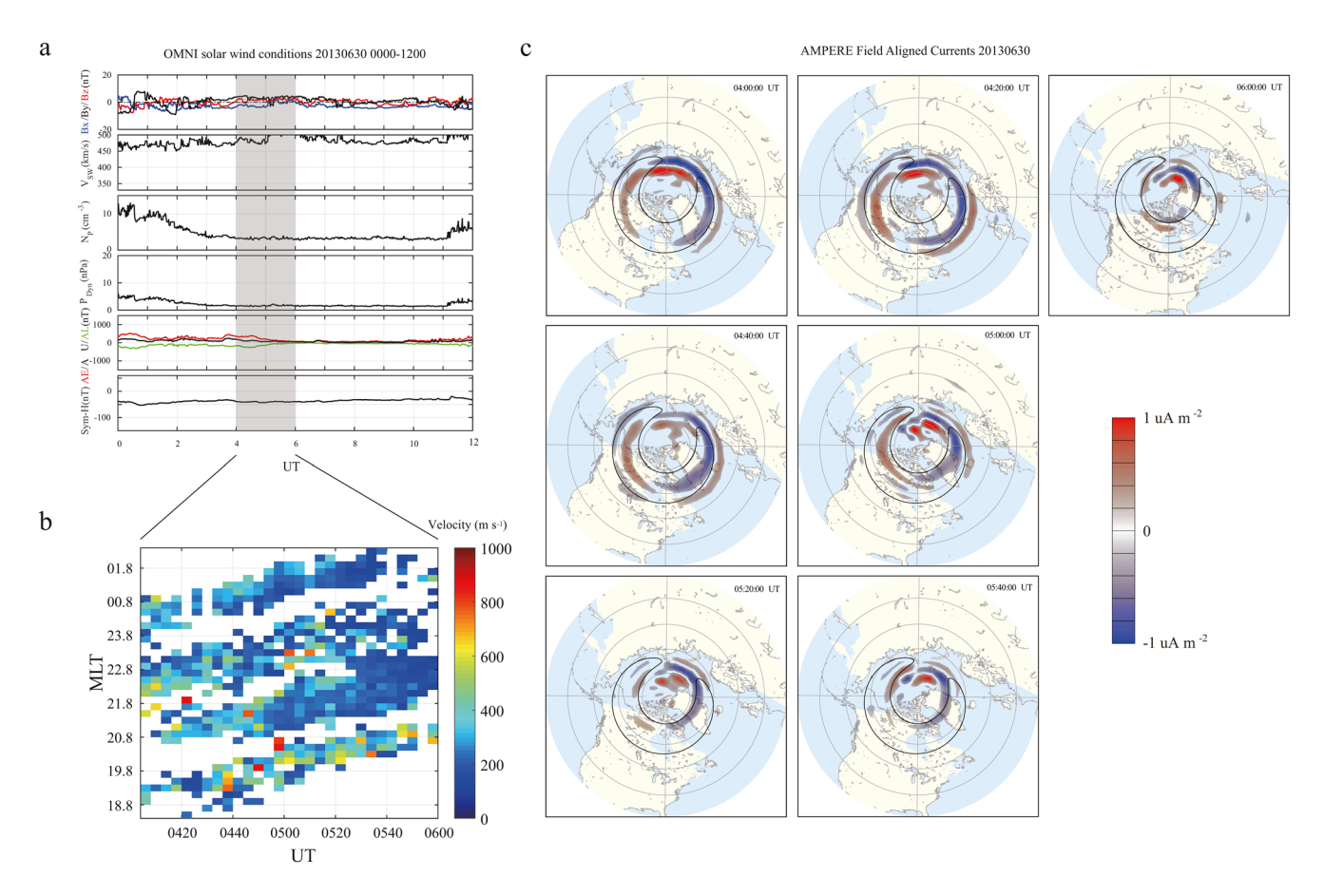


Figure 5. The same format as Figure 3 but for the June 30, 2013 case.

cross the pre-dusk side during the observation period that is also a difficulty to estimate the FACs around the 1900–2100 MLT region. We know that the R2 FACs provide the basic condition for generating the SAPS channel around dusk side, so we infer that in that region, the R2 FACs are weak which also corresponded well with the status of the SAPS velocity.

Figure 5a shows the solar wind conditions on June 30, 2013. A magnetic storm occurs during June 28-30, 2013 with the lowest SYMH index of -100 nT at \sim 0700 UT on June 29. On June 30, the recovery phase lasts for almost the whole day. The June 30, 2013 case occurs at the end of the magnetic storm recovery phase with the SYMH index about -40 nT, which is almost similar with the quiet time of the magnetic disturbance. AE index shows that this case also happens in the recovery phase of a weak substorm (the maximum AE index is ~400 nT). The IMF Bz is totally northward (>0 nT) during the period which is different from that of the first two cases. Figure 5b shows the velocity distributions in MLT/UT grids. From 0400 to 0600 UT, the velocity distribution is discrete and broken. There is no obvious feature of velocity from dusk side to midnight side that is quite different compared to the first two cases (from dusk side to midnight side, the velocity decreases). Overall, the total velocity considering all of MLTs also decreases with UT. Before 0500 UT, the velocity is about $300-500 \text{ m s}^{-1}$; after 0500 UT, the velocity decreases into about $200-300 \text{ m s}^{-1}$. The velocity decrease in this case is similar with the SYMH and AE indices of magnetic storm and substorm recovery phase. However, though both cases on October 25, 2011 and June 28-30, 2013 happen during the recovery phases, the variations of velocity along the MLT are quite different. We notice that the IMFs in both these cases are also different. The Bz is southward in the October 25, 2011 case while it is northward in June 28-30, 2013. According to previous studies, the SAPS are dynamic and respond quickly to IMF (e.g., He et al., 2018; Oksavik et al., 2006). Somewhat different evolution patterns of SAPS are presented by He et al. (2017) using DMSP instruments. In their study, the relation between the duration of SAPS and the duration of southward IMF shows a good correlation with a coefficient of 0.99. When the IMFs are northward,

ZHANG ET AL. 8 of 16



the SAPS velocity structures are discontinuous and discrete as shown in Figure 5b. Besides, the relation between SAPS velocity and MLT also disappears. Figure 5c shows the FACs map on June 28–30, 2013. Compared with the first two cases, the FACs in this case are much weaker and the regions of the FACs are contractive. Without enough support of the R2 FACs in subauroral region, the SAPS channels are broken and the SAPS velocity distribution becomes discontinuous.

In general, the SAPS velocity shows similar variations with the magnetic activities. As magnetic activities enhance, the SAPS velocity increases; and as the magnetic activities fade away, the SAPS velocity decreases. The relations between the evolution of SAPS velocity and geomagnetic indices especially the SYMH index show similar result as shown in previous statistical studies (e.g., Erickson et al., 2011; Kunduri et al., 2017). Besides, it seems that SAPS velocity variations are very similar to the evolution of the magnetic storms. As shown by the observations, the increase of SAPS velocity first appears around the dusk side (~1800–2100 MLT), and expands to midnight side as SYMH index decreases during the storm main phase, and then shrinks back to the dusk side with decreasing speed as SYMH index increases during the storm recovery phase. Finally, the SAPS velocity distribution is broken and becomes discontinuous in the end of the magnetic storm. We know that the SAPS velocity is basically driven by the ring current pressure gradients. The ring current energy injects into the ionosphere low conductivity subauroral regions through R2 FACs, which generates the SAPS channel by polarization drift (e.g., Anderson, 2004; Anderson et al., 1993; Yeh et al., 1991). Considering the influence to the ring current, SAPS velocity variations show very similar behaviors with the magnetic storm. The result indicates that our observations confirm the SAPS generation mechanism proposed by prior authors. Besides, an inference can be included such as the forceful influences of the ring current on SAPS happen around the dusk side, and then appear and enhance in other MLT regions; similarly, the dusk side is the last region where the influence of ring current fade away. Lin et al. (2019) model the large-scale evolution of SAPS using coupled magnetosphere-ionosphere-thermosphere model. The simulation shows a large-scale (post-noon side to midnight side) SAPS evolve in the complete period of a major magnetic storm. The velocity distribution in their simulation shows strong relation with the magnetic storm. Our observation shows similarities with the velocity distribution variations in their simulation (The variations of SAPS velocity first appear around the dusk side; expand to other MLTs, and shrink back to dusk side). Besides, when the southward IMFs are weak or turn to northward, the SAPS structures also show discontinuities in their simulation. Although our cases occur in different magnetic storm events, it can also reveal the velocity evolution of SAPS. Our observations partly confirm the validity of the simulative results and the strong influences of the magnetic storms.

2.5. Geomagnetic Activity Dependence of SAPS

It may be noted that there is an important feature of the longitudinal velocity variations in SAPS evolution. SAPS are narrow and highly dynamic flows covering the longitudinal regions from post-noon side to post-dawn. Therefore, it appears there is a need of a parameter to describe the intensity of the SAPS flow longitudinal transport because of the large difference of velocity magnitude with the MLTs. In Figure 6, we present the relation between SAPS velocity and MLT during 0508–0512 UT. SAPS velocity has a similar linear correlation with the MLT which is proposed by previous studies. However, the linear correlation has small difference with the results of Clausen et al. (2012) and Kunduri et al. (2017). The difference seems acceptable in statistics. In our study, the linear fitting is applied to the relation between the SAPS velocity and the MLT as done earlier by Erickson et al. (2011). The blue solid squares and error bars show the mean values and deviations. We calculate the mean values in each MLT to represent the SAPS velocity in that MLT. The red solid line is the linear fitting line. The slope is calculated based on 1 MLAT/0.2 MLT grids, so the unit of the slope is m s⁻¹/0.2 mlt. From 1836 to 0236 MLT, the SAPS flows transport is quite unbalanced. Most part of the longitudinal transport is provided by that around dusk side. The slope is defined as the intensity of SAPS longitudinal transport. The smaller the slopes, the more intense the SAPS flows transport.

Figure 7 shows the correlations between T-Slope/SAPS velocity and the three geomagnetic indices SYMH/AE/Bz in the February 19, 2014 case. Figures 7a–7c show the SYMH, AE/AU/AL indices, and IMF conditions on that day. The shaded areas show the periods of interest. Figures 7d–7f show the T-slope (SAPS velocity longitudinal tendency, represent the intensity of SAPS longitudinal transport) and the SYMH/AE/Bz changing with UT. Figures 7g–7i show the correlations between T-Slope and SYMH/AE/Bz. Figures 7j–7l

ZHANG ET AL. 9 of 16

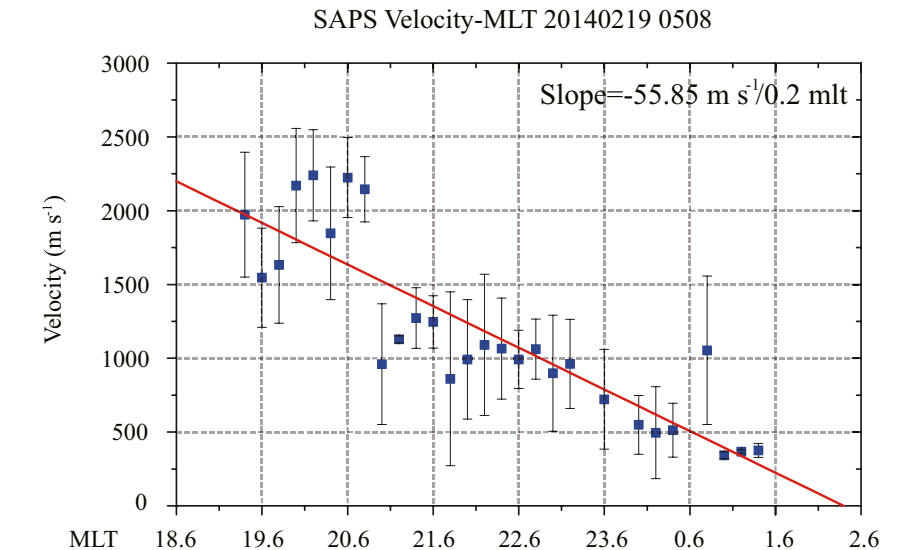


Figure 6. The distribution of subauroral polarization streams (SAPS) velocity with MLT in 0508–0512 UT. The blue solid squares and errorbars show the mean values and deviations at the same MLT. The red solid line shows the linear fitting. The x axis represents the MLT. The y axis represents the velocity. The linear fitting slope is -55.85 m s $^{-1}/0.2$ mlt.

show the correlations between SAPS velocity and the three indices. The value is calculated as the mean velocity in all MLT in each time segment. We first consider the SYMH index. Figure 7d shows the T-slope and the SYMH index changing with UT. The variations of the two are almost the same: increasing with UT. All of the T-Slopes are negative that obey the rule found by previous studies (SAPS velocity decreases with the MLT). We notice that around 0425 UT (marked by dotted line), both of the T-Slope and SYMH index start to increase steeply from the steady states. It indicates that the response of SAPS to the magnetic storm is prompt. From Figure 7g, we find that there is a good linear correlation between the T-Slope and SYMH index with a coefficient of 0.89. Besides, the good linear correlation between SAPS velocity and SYMH index is also found in Figure 7j (R = -0.85). The result indicates that the responses of the SAPS velocity are prompt and intense during the main phase of the magnetic storm; and the intense SAPS flow transport is mainly provided by the dusk side transport; the SAPS velocity variation is almost dominated by the magnetic storm. At the same time, a large substorm is developing during the growth phase with AE index of ~1,000 nT. In Figure 7e, both of the T-Slope and AE also show the increases with UT while the AE index is strongly disturbed. The large variations of the two also happen around 0425 UT. However, the linear fitting coefficient between the two is about -0.49 in Figure 7h which shows a moderate correlation while that of SYMH index shows a good correlation. Furthermore, the SAPS velocity has a comparatively poor linear correlation with AE in Figure 7k (R = 0.43). The result indicates that the impact of the substorm to the SAPS velocity is weaker in comparison to that of magnetic storm. The similar results have also been found with the Bz. In Figure 7f, the Bz is approximately invariant and lasted for most of time (~0410-0455 UT, ~25 nT). Although the southward IMFs provide good dayside magnetic reconnection conditions, the T-Slope and IMF Bz show different behaviors. The linear correlations between T-Slope/SAPS velocity and Bz in Figures 7i and 7l are also poor with the coefficients of -0.14/0.22. The result shows that in this case the Bz has no obvious correlation with the SAPS velocity, though the negative Bz provides good magnetic conditions. Overall, the SAPS velocity during the magnetic storm main phase has a good linear correlation with SYMH index and the similar variations of the T-Slope and SYMH index show that the dominance is prominent. Considering the AE/Bz, the influences of substorm/IMF to the SAPS velocity are much weaker in comparison to that of magnetic storm.

Figure 8 shows the same format as Figure 7 but for the October 25, 2011 case. Compared with the February 19, 2014 case, this case occurs in recovery phase of a large magnetic storm. In Figure 8d, although all of the T-Slopes are negative, the values are larger compared to that of the February 19, 2014 case. Most of the T-Slopes maintain at \sim -10 which indicates that the SAPS longitudinal transport is relative stable. Meanwhile, the SYMH index shows slight increase from \sim 130 to \sim 122 nT. The linear fitting between T-Slope and

ZHANG ET AL. 10 of 16



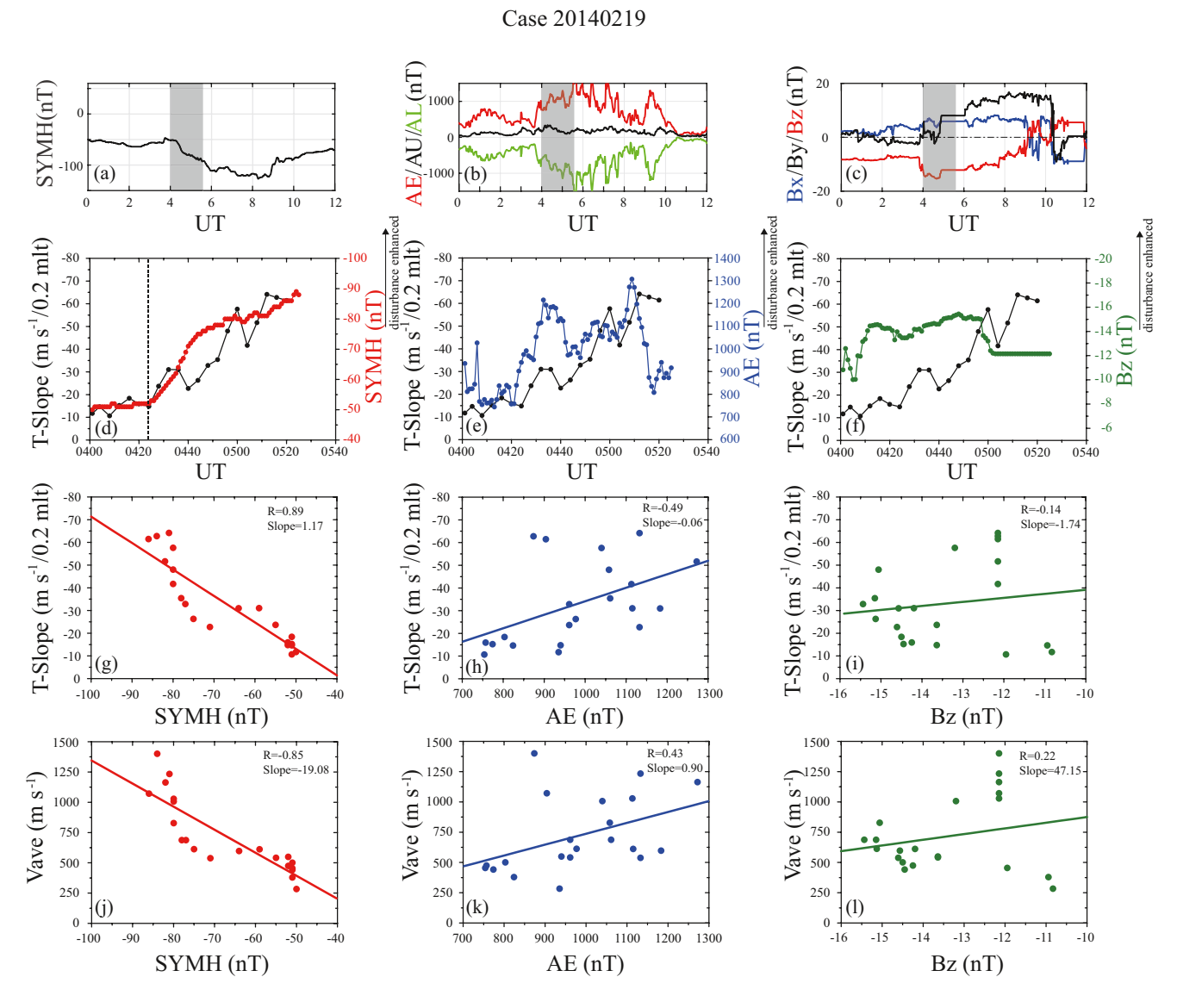


Figure 7. The solar wind conditions and correlations between T-Slope/subauroral polarization streams (SAPS) velocity and the three geomagnetic indices (SYMH/AE/Bz) in the February 19, 2014 case. (a–c) The SYMH, AU/AE/AL and IMF along with UT. The shaded areas show the periods of interest. (d–f) The T-Slope and the SYMH/AE/Bz along with UT. (g–i) The correlations between T-Slope and SYMH/AE/Bz. (j–l) The correlations between SAPS velocity (V_{ave}) and SYMH/AE/Bz.

SYMH index is poor in Figure 8g (R=-0.2). Considering the increases of SAPS velocity are shrinking back to around the dusk side in this case, the intensity of the SAPS longitudinal transport slightly enhances from stable states. It is worth noting that, even during the recovery phase with decreased velocity, the most part of the SAPS longitudinal transport is also provided by the dusk side transport. Surprisingly, the linear fitting between SAPS velocity and SYMH index is still good with a coefficient of -0.76 in Figure 8j. We also notice that the fitting slopes in both of the first two cases are similar (-19.08 in February 19, 2014 case and -21.19 in October 25, 2011 case). It indicates that even though in different magnetic conditions, the linear correlation still exists although the SAPS velocity magnitude is quite different. The AE index shows small changes with UT in Figure 8e and the linear fitting is weak between T-Slope and AE index in Figure 8h. However, there is a moderate linear correlation between SAPS velocity and AE index in Figure 8k (R=0.53). Similarly, in Figure 8l, the moderate linear correlation is also found between the SAPS velocity and Bz (R=-0.60) that is similar to the correlation provided by Lin et al. (2019) (R=-0.57). Both these correlations in Figures 8k and 8l are quite different with that of the February 19, 2014 case. The results indicate that during

ZHANG ET AL. 11 of 16



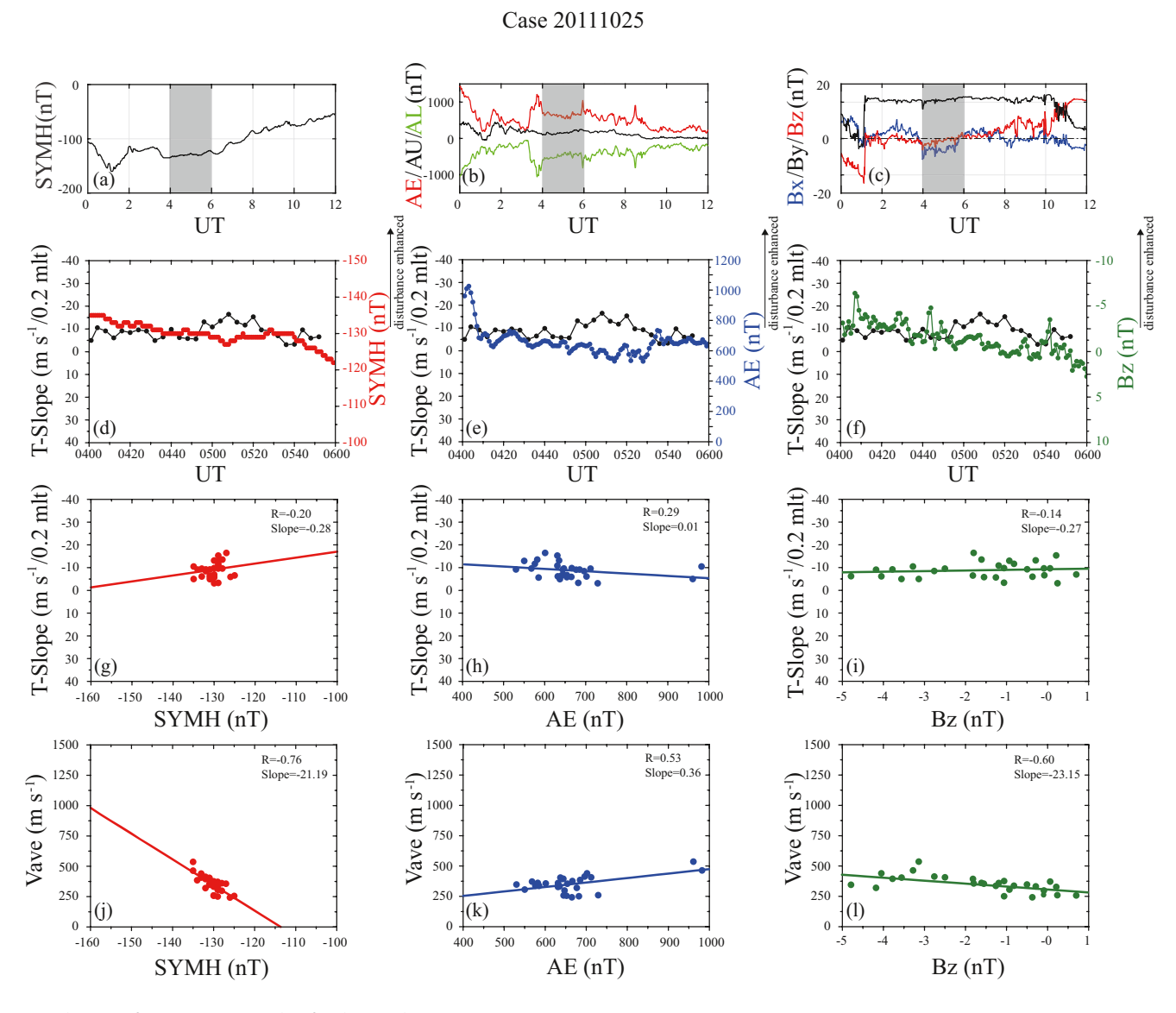


Figure 8. The same format as Figure 7 but for the October 25, 2011 case.

the recovery phase of the large magnetic storm (-100 to -200 nT), the substorm and IMF can also affect the SAPS velocity although the amplitude of SAPS velocity is only about 200 m s^{-1} . In comparison to the case of February 19, 2014, the dominance of the substorm and IMF to the SAPS velocity gradually appears in the recovery phase. The factors affecting the SAPS magnitude are not restricted to the SYMH index but also AE, Bz, and magnetic storm phases.

We discuss further the situation during the end of a magnetic storm. Figure 9 shows the same format as Figure 7 but for the June 30, 2013 case. The obvious difference with the first two cases is that most of the T-Slopes are positive which means the SAPS velocity does not always follow the Velocity-MLT rule (SAPS velocity decrease with the MLT). The three indices show different variations compared to that of the T-Slope in Figures 9d–9f, indicating that the SAPS flow transport is chaotic. In this case, the SYMH is almost invariable; AE shows the recovery phase of a weak substorm (~400 nT); and Bz is mainly northward (>0 nT). He et al. (2017) propose that the southward IMF duration is generally consistent with the duration of the SAPS statistically. SAPS are strongly responsive to the southward IMF. Meanwhile, in Lin's simulation, when the southward IMF is weak, SAPS become discontinuous. The strong dependence to the IMF causes the chaos in T-Slope distribution. Similarly, the T-Slope has poor correlations with the three indices in Figures 9g–9i.

ZHANG ET AL. 12 of 16

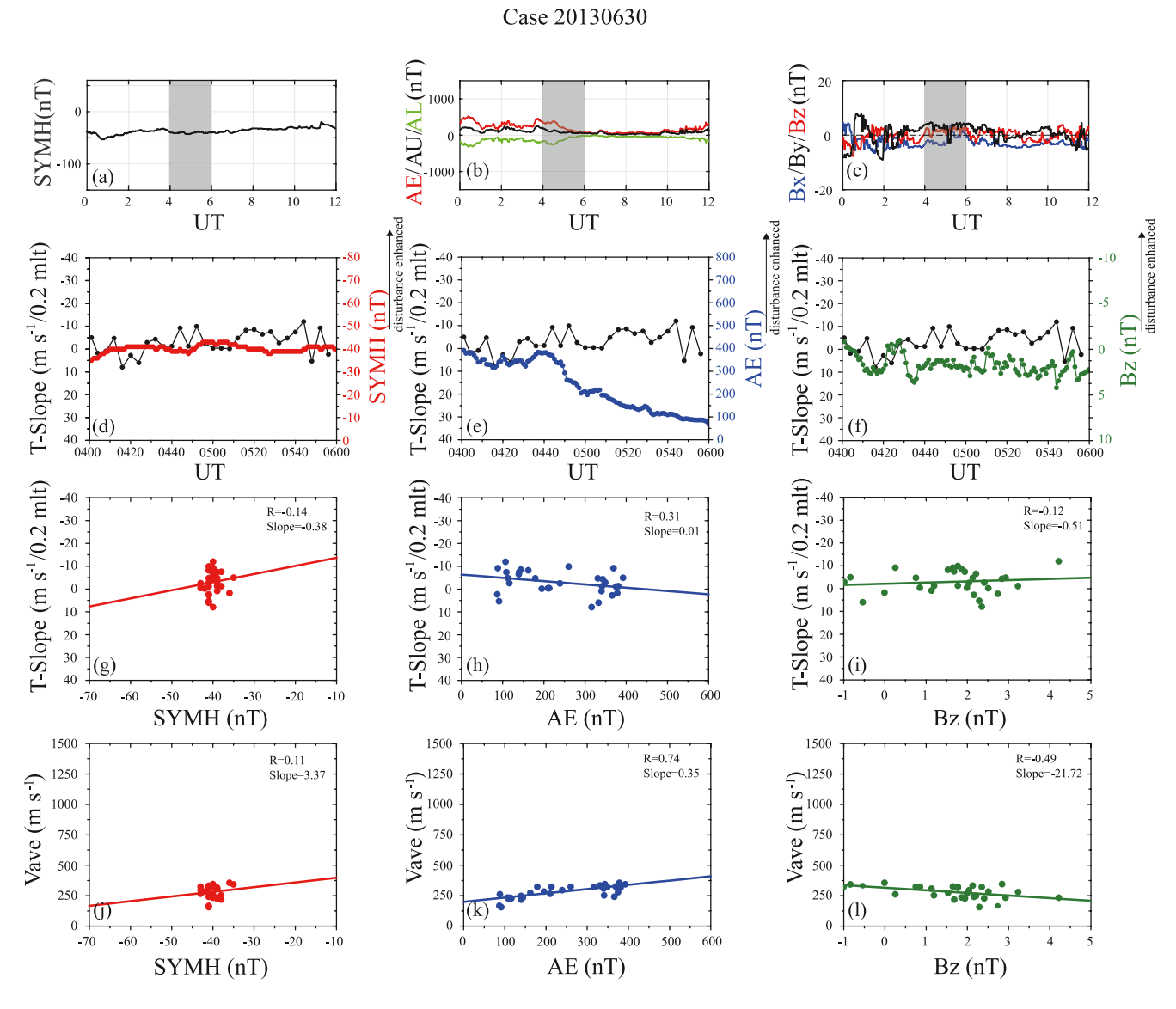


Figure 9. The same format as Figure 7 but for the June 30, 2013 case.

With the weak dominance of the magnetic storm on SAPS, the SAPS velocity no longer has a good correlation with the SYMH index as Figure 9j shows. However, the moderate correlations with AE/Bz also exist in Figures 9k and 9l compared to Figures 8k and 8l. The SAPS velocity has moderate linear correlations with AE index and Bz though the amplitude of SAPS velocity is still small. The results indicate that at the end of the magnetic storm process, the dominance of magnetic storm has disappeared, instead, the dominance of substorm and IMF still exists on the SAPS velocity manifesting as moderate linear correlations between SAPS velocity and AE/Bz.

3. Discussion and Summary

In this study, we present the observations of the evolution of SAPS in different conditions and magnetic storm phases. Because of the observation limitations, the three cases have been observed in short time durations (1.5–2 h) in three magnetic storm, and the observations are from the dusk side to midnight regions. However, we can get valuable features of the SAPS evolution. SAPS velocity is dominated by the strong ring current injection during magnetic storms; response of the SAPS velocity to the magnetic storm is prompt,

ZHANG ET AL. 13 of 16



Acknowledgments

This work was supported by the Nation-

al Science Foundation of China (grants

41674173 and 41904152), the Special-

ized Research Fund for State Key lab-

oratory of China and the pre-research

project on Civil Aerospace Technologies

No. D020104 funded by China's Nation-

al Space Administration. The work at

Shandong University was supported

the Specialized Research Fund for

netic Environment, and the Chinese

Meridian Project. The authors thank

Polar Research Institute of China for

providing a computing server and Su-

perDARN data. The authors thank the

NOAA FTP and JHU/APL for making

available the DMSP data (https://satdat.

ngdc.noaa.gov/dmsp/data/) and SSUSI

auroral data and model (https://ssusi.

jhuapl.edu). The authors thank the

NASA OMNIWeb for the solar wind

and IMF data. The authors thank the

Iridium-derived data products (http://

html). The authors also thank Prof. He

Fei from Institute of Geology and Geo-

physics, Chinese Academy of Sciences for great help in daily discussions. The

authors also thank Prof. Balan Nanan

for improving the language and useful

discussion.

ampere.jhuapl.edu/rBrowse/index.

AMPERE team and the AMPERE

Science Center for providing the

by the National Science Foundation of

China (grants 41874170 and 41604139),

National Key Laboratory of Electromag-

especially for the intense magnetic activities (such as the main phase of magnetic storm). During the main phase, the increases of the SAPS velocity first appear around the dusk side; then with the enhancement of the magnetic storm, the increases expand to other MLTs. During the recovery phase, the SAPS velocity decreases and starts to shrink back to around the dusk side. In the end of a magnetic storm, with the northward IMF, the SAPS velocity distribution becomes broken and is discontinuous along with the MLTs.

The correlations in specific cases between the SAPS velocity and the geomagnetic indices are quite different. Because of the different magnetic conditions, the lower SYMH index can also correspond to the lower SAPS velocity as shown in Figures 7j and 8j. The factors impacting the SAPS velocity magnitude are multiple, such as IMF, AE, and phases of magnetic storms. During strong magnetic storm conditions (main phase), the SAPS velocity has a good linear correlation with SYMH index in the evolution process but weak correlations with AE/Bz. The effect of the magnetic storm to SAPS velocity is much stronger than that of the substorm/IMF. However, when the magnetic storm becomes gentle (recovery phase), good linear correlations appear between SAPS velocity and AE/Bz; besides, the good correlation between SAPS velocity and SYMH index still exists. When the disturbance of magnetic storm becomes weak (end of the recovery phase), the good correlation with the SYMH index disappears, but exists with AE/Bz.

Data Availability Statement

Raw files can also be accessed via the SuperDARN data mirrors hosted by the British Antarctic Survey (https://www.bas.ac.uk/project/superdarn/#data) and University of Saskatchewan (https://superdarn.ca).

References

- Aa, E., Erickson, P. J., Zhang, S.-R., Zou, S., Coster, A. J., Goncharenko, L. P., & Foster, J. C. (2020). A statistical study of the subauroral polarization stream over North American sector using the Millstone Hill incoherent scatter radar 1979–2019 measurements. *Journal of Geophysical Research: Space Physics*, 125, e2020JA028584. https://doi.org/10.1029/2020JA028584
- Anderson, B. J., Takahashi, K., & Toth, B. A. (2000). Sensing global Birkeland currents with Iridium engineering magnetometer data. Geophysical Research Letters, 27, 4045–4048. https://doi.org/10.1029/2000GL000094
- Anderson, P. C. (2004). Subauroral electric fields and magnetospheric convection during the April 2002 geomagnetic storms. *Geophysical Research Letters*, 31, L11801. https://doi.org/10.1029/2004GL019588
- Anderson, P. C., Carpenter, D. L., Tsuruda, K., Mukai, T., & Rich, F. J. (2001). Multisatellite observations of rapid subauroral ion drifts (SAID). Journal of Geophysical Research, 106(A12), 29585–29599. https://doi.org/10.1029/2001JA000128
- Anderson, P. C., Hanson, W. B., Heelis, R. A., Craven, J. D., Baker, D. N., & Frank, L. A. (1993). A proposed production model of rapid subauroral ion drifts and their relationship to substorm evolution. *Journal of Geophysical Research*, 98(A4), 6069–6078. https://doi.org/10.1029/92JA01975
- Anderson, P. C., Heelis, R. A., & Hanson, W. B. (1991). The ionospheric signatures of rapid subauroral ion drifts. *Journal of Geophysical Research*, 96(90), 5785–5792. https://doi.org/10.1029/90JA02651
- Buonsanto, M. J., Foster, J. C., & Sipler, D. P. (1992). Observations from Millstone Hill during the geomagnetic disturbances of March and April 1990. *Journal of Geophysical Research*, 97(A2), 1225. https://doi.org/10.1029/91JA02428
- Chisham, G., Lester, M., Milan, S. E., Freeman, M. P., Bristow, W. A., Grocott, A., et al. (2007). A decade of the Super Dual Auroral Radar Network (SuperDARN): Scientific achievements, new techniques, and future directions. Surveys in Geophysics, 28(1), 33–109. https://doi.org/10.1007/s10712-007-9017-8
- Clausen, L. B. N., Baker, J. B. H., Ruohoniemi, J. M., Greenwald, R. A., Thomas, E. G., Shepherd, S. G., et al. (2012). Large-scale observations of a subauroral polarization stream by midlatitude superDARN radars: Instantaneous longitudinal velocity variations. *Journal of Geophysical Research*, 117, A05306. https://doi.org/10.1029/2011JA017232
- Dungey, J. W. (1961). Interplanetary magnetic field and the auroral zones. *Physical Review Letters*, 6, 47–48. https://doi.org/10.1103/physrevlett.6.47
- Ebihara, Y., Nishitani, N., Kikuchi, T., Ogawa, T., Hosokawa, K., & Fok, M.-C. (2008). Two-dimensional observations of overshielding during a magnetic storm by the Super Dual Auroral Radar Network (SuperDARN) Hokkaido radar. *Journal of Geophysical Research*, 113, A01213. https://doi.org/10.1029/2007JA012641
- Erickson, P. J., Beroz, F., & Miskin, M. Z. (2011). Statistical characterization of the American sector subauroral polarization stream using incoherent scatter radar. *Journal of Geophysical Research*, 116, A00J21. https://doi.org/10.1029/2010JA015738
- Erickson, P. J., Goncharenko, L. P., Nicolls, M. J., Ruohoniemi, M., & Kelley, M. C. (2010). Dynamics of North American sector ionospheric and thermospheric response during the November 2004 superstorm. *Journal of Atmospheric and Solar-Terrestrial Physics*, 72(4), 292–301.
- Foster, J. C., & Burke, W. J. (2002). SAPS: A new categorization for sub-auroral electric fields. Eos Transactions American Geophysical Union, 83(36), 393–394. https://doi.org/10.1029/2002EO000289
- Foster, J. C., Coster, A. J., Erickson, P. J., Holt, J. M., Lind, F. D., Rideout, W., et al. (2005). Multiradar observations of the polar tongue of ionization. *Journal of Geophysical Research*, 110, A09S31. https://doi.org/10.1029/2004JA010928
- Foster, J. C., Erickson, P. J., Lind, F. D., & Rideout, W. (2004). Millstone Hill coherent-scatter radar observations of electric field variability in the sub-auroral polarization stream. *Geophysical Research Letters*, 31, L21803. https://doi.org/10.1029/2004GL021271
- Foster, J. C., & Vo, H. B. (2002). Average characteristics and activity dependence of the subauroral polarization stream. *Journal of Geophysical Research*, 107(A12), 1475. https://doi.org/10.1029/2002JA009409
- $Galperin, Y., Ponomarev, V. N., \&\ Zosimova, A.\ G.\ (1974).\ Plasma\ convection\ in\ the\ polar\ ionosphere.\ Annales\ Geophysicae,\ 30,\ 1-7.$

ZHANG ET AL. 14 of 16

- Greenwald, R. A., Baker, K. B., Dudeney, J. R., Pinnock, M., Jones, T. B., Thomas, E. C., et al. (1995). Darn/SuperDARN: A global view of the dynamics of high-latitude convection. Space Science Reviews, 71(71), 761–796. https://doi.org/10.1007/BF00751350
- Hanuise, C., Senior, C., Cerisier, J. C., Villain, J. P., Greenwald, R. A., Ruohoniemi, J. M., & Baker, K. B. (1993). Instantaneous mapping of high-latitude convection with coherent HF radars. *Journal of Geophysical Research*, 98(A10), 17387–17400. https://doi.org/10.1029/93JA00813
- He, F., Zhang, X., Wang, W., & Wan, W. (2017). Different evolution patterns of subauroral polarization streams (SAPS) during intense storms and quiet time substorms. *Geophysical Research Letters*. 44, 10796–10804. https://doi.org/10.1002/2017GL075449
- He, F., Zhang, X.-X., & Chen, B. (2014). Solar cycle, seasonal, and diurnal variations of subauroral ion drifts: Statistical results. *Journal of Geophysical Research: Space Physics*, 119, 5076–5086. https://doi.org/10.1002/2014JA019807
- He, F., Zhang, X.-X., Wang, W., & Chen, B. (2016). Double-peak subauroral ion drifts (DSAIDs). Geophysical Research Letters, 43, 5554–5562. https://doi.org/10.1002/2016GL069133
- He, F., Zhang, X.-X., Wang, W., Liu, L., Ren, Z.-P., Yue, X., et al. (2018). Large-scale structure of subauroral polarization streams during the main phase of a severe geomagnetic storm. *Journal of Geophysical Research: Space Physics*, 123, 2964–2973. https://doi.org/10.1002/2018JA025234
- He, F., Zhang, X.-X., Wang, W., Pu, Z.-Y., Zong, Q.-G., Yao, Z., et al. (2019). Evolution of the subauroral polarization stream oscillations during the severe geomagnetic storm on November 20, 2003. *Geophysical Research Letters*, 46, 599–607. https://doi.org/10.1029/2018GL081446
- Heelis, R. A., Bailey, G. J., Sellek, R., Moffett, R. J., & Jenkins, B. (1993). Field-aligned drifts in subauroral ion drift events. *Journal of Geophysical Research*, 98(A12), 21493–21499. https://doi.org/10.1029/93JA02209
- Horvath, I., & Lovell, B. C. (2017). Investigating the development of double-peak subauroral ion drift (DSAID). *Journal of Geophysical Research: Space Physics*, 122, 4526–4542. https://doi.org/10.1002/2016JA023506
- Horvath, I., & Lovell, B. C. (2018). Investigating the development of abnormal subauroral ion drift (ASAID) and abnormal subauroral polarization stream (ASAPS) during the magnetically active times of September 2003. *Journal of Geophysical Research: Space Physics*, 123, 1566–1582. https://doi.org/10.1002/2017JA024870
- Horvath, I., & Lovell, B. C. (2021). Investigating the development of distinctive subauroral flow channels during the November 7–8, 2004 Superstorm. *Journal of Geophysical Research: Space Physics*, 126, e2020JA027821. https://doi.org/10.1029/2020JA027821
- Huang, C. S., & Foster, J. C. (2007). Correlation of the subauroral polarization streams (SAPS) with the Dst index during severe magnetic storms. *Journal of Geophysical Research*, 112, A11302. https://doi.org/10.1029/2007JA012584
- Karlsson, T., Marklund, G. T., Blomberg, L. G., & Mälkki, A. (1998). Subauroral electric fields observed by the Freja satellite: A statistical study. Journal of Geophysical Research, 103(A3), 4327–4341. https://doi.org/10.1029/97ja00333
- Kunduri, B. S. R., Baker, J. B. H., Ruohoniemi, J. M., Nishitani, N., Oksavik, K., Erickson, P. J., et al. (2018). A new empirical model of the subauroral polarization stream. *Journal of Geophysical Research: Space Physics*, 123, 7342–7357. https://doi.org/10.1029/2018JA025690
- Kunduri, B. S. R., Baker, J. B. H., Ruohoniemi, J. M., Thomas, E. G., Shepherd, S. G., & Sterne, K. T. (2017). Statistical characterization of the large-scale structure of the sub-auroral polarization stream. *Journal of Geophysical Research: Space Physics*, 122, 6035–6048. https://doi.org/10.1002/2017JA024131
- Liléo, S., Karlsson, T., & Marklund, G. T. (2010). Statistical study on the occurrence of ASAID electric fields. Annales Geophysicae, 28, 439–448. https://doi.org/10.5194/angeo-28-439-2010
- Lin, D., Wang, W., Scales, W. A., Pham, K., Liu, J., Zhang, B., et al. (2019). SAPS in the March 17, 2013 storm event: Initial results from the coupled magnetosphere-ionosphere-thermosphere model. *Journal of Geophysical Research: Space Physics*, 124, 6212–6225. https://doi.org/10.1029/2019JA026698
- Ma, Y.-Z., Zhang, Q.-H., Xing, Z.-Y., Jayachandran, P. T., Moen, J., Heelis, R. A., & Wang, Y. (2018). Combined contribution of solar illumination, solar activity, and convection to ion upflow above the polar cap. *Journal of Geophysical Research: Space Physics*, 123, 4317–4328. https://doi.org/10.1029/2017JA024974
- Morrison, D., Paxton, L. J., Humm, D. C., Wolven, B., Meng, C. I., Zhang, Y., et al. (2002). On-orbit calibration of the Special Sensor Ultraviolet Scanning Imager (SSUSI): A far-UV imaging spectrograph on DMSP F-16. Proceedings of SPIE. https://doi.org/10.1117/12.454267
- Oksavik, K., Greenwald, R. A., Ruohoniemi, J. M., Hairston, M. R., Paxton, L. J., Baker, J. B. H., et al. (2006). First observations of the temporal/spatial variation of the sub-auroral polarization stream from the SuperDARN Wallops HF radar. *Geophysical Research Letters*, 33, L12104. https://doi.org/10.1029/2006GL026256
- Paxton, L. J., Morrison, D., Zhang, Y., Kil, H., Meng, C. I., Ogorzalek, B. S., et al. (2002). Validation of remote sensing products produced by the Special Sensor Ultraviolet Scanning Imager (SSUSI): A far UV-imaging spectrograph on DMSP F-16. Proceedings of SPIE. https://doi.org/10.1117/12.454268
- Ruohoniemi, J. M., Greenwald, R. A., Baker, K. B., Villain, J. P., Hanuise, C., & Kelly, J. (1989). Mapping high-latitude plasma convection with coherent HF radars. *Journal of Geophysical Research*, 94(A10), 13463–13477. https://doi.org/10.1029/JA094iA10p13463
- Schunk, R. W., Banks, P. M., & Raitt, W. J. (1976). Effects of electric fields and other processes upon the nighttime high-latitude F layer. Journal of Geophysical Research, 81(19), 3271–3282. https://doi.org/10.1029/JA081i019p03271
- Spiro, R. W., Heelis, R. A., & Hanson, W. B. (1979). Rapid subauroral ion drifts observed by atmosphere Explorer C. Geophysical Research Letters, 6, 657–660. https://doi.org/10.1029/GL006i008p00657
- Villain, J. P., Greenwald, R. A., Baker, K. B., & Ruohoniemi, J. M. (1987). HF radar observations of E region plasma irregularities produced by oblique electron streaming. *Journal of Geophysical Research*, 92(A11), 12327–12342. https://doi.org/10.1029/JA092iA11p12327
- Voiculescu, M., & Roth, M. (2008). Eastward sub-auroral ion drifts or ASAID. Annales Geophysicae, 26, 1955–1963. https://doi.org/10.5194/angeo-26-1955-2008
- Wang, H., & Lühr, H. (2013). Seasonal variation of the ion upflow in the topside ionosphere during SAPS (subauroral polarization stream) periods. *Annales Geophysicae*, 31, 1521–1534. https://doi.org/10.5194/angeo-31-1521-2013
- Wang, H., Lühr, H., Häusler, K., & Ritter, P. (2011). Effect of subauroral polarization streams on the thermosphere: A statistical study. Journal of Geophysical Research, 116, A03312. https://doi.org/10.1029/2010JA016236
- Wang, H., Ridley, A. J., Lühr, H., Liemohn, M. W., & Ma, S. Y. (2008). Statistical study of the subauroral polarization stream: Its dependence on the cross-polar cap potential and subauroral conductance. *Journal of Geophysical Research*, 113, A12311. https://doi.org/10.1029/2008JA013529
- Wang, Z., Zou, S., Shepherd, S. G., Liang, J., Gjerloev, J. W., Ruohoniemi, J. M., et al. (2019). Multi-instrument observations of mesoscale enhancement of subauroral polarization stream associated with an injection. *Journal of Geophysical Research: Space Physics*, 124, 1770–1784. https://doi.org/10.1029/2019JA026535
- Waters, C. L., Anderson, B. J., & Liou, K. (2001). Estimation of global field aligned currents using the Iridium system magnetometer data. Geophysical Research Letters, 28, 2165–2168. https://doi.org/10.1029/2000gl012725

ZHANG ET AL. 15 of 16



- Yeh, H.-C., & Foster, J. C. (1990). Storm time heavy ion outflow at mid-latitude. *Journal of Geophysical Research*, 95(A6), 7881–7891. https://doi.org/10.1029/JA095iA06p07881
- Yeh, H.-C., Foster, J. C., Rich, F. J., & Swider, W. (1991). Storm time electric field penetration observed at mid-latitude. *Journal of Geophysical Research*, 96(A4), 5707–5721. https://doi.org/10.1029/90ja02751
- Yuan, Z. G., Deng, X. H., & Wang, J. F. (2008). DMSP/GPS observations of intense ion upflow in the midnight polar ionosphere associated with the SED plume during a super geomagnetic storm. *Geophysical Research Letters*, 35(19), L19110. https://doi.org/10.1029/2008GL035462
- Zhang, Q.-H., Lockwood, M., Foster, J. C., Zhang, S.-R., Zhang, B.-C., McCrea, I. W., et al. (2015). Direct observations of the full Dungey convection cycle in the polar ionosphere for southward interplanetary magnetic field conditions. *Journal of Geophysical Research: Space Physics*, 120, 4519–4530. https://doi.org/10.1002/2015JA021172
- Zhang, Q.-H., Ma, Y. Z., Jayachandran, P. T., Moen, J., Lockwood, M., Zhang, Y.-L., et al. (2017). Polar cap hot patches: Enhanced density structures different from the classical patches in the ionosphere. *Geophysical Research Letters*, 44, 8159–8167. https://doi. org/10.1002/2017GL073439
- Zhang, Q.-H., Zhang, B.-C., Liu, R.-Y., Dunlop, M. W., Lockwood, M., Moen, J., et al. (2011). On the importance of interplanetary magnetic field n polar cap patch formation. *Journal of Geophysical Research*, 116, A05308. https://doi.org/10.1029/2010JA016287
- Zhang, Q.-H., Zhang, B. C., Lockwood, M., Hu, H. Q., Moen, J., Ruohoniemi, J. M., et al. (2013). Direct observations of the evolution of polar cap ionization patches. *Science*, 339(6127), 1597–1600. https://doi.org/10.1126/science.1231487
- Zhang, Q.-H., Zong, Q.-G., Lockwood, M., Heelis, R. A., Hairston, M., Liang, J., et al. (2016). Earth's ion upflow associated with polar cap patches: Global and in situ observations. *Geophysical Research Letters*, 43, 1845–1853. https://doi.org/10.1002/2016GL067897
- Zhang, Q., Liu, Y. C.-M., Zhang, Q.-H., Xing, Z.-Y., Wang, Y., & Ma, Y.-Z. (2020). Statistical study of ion upflow associated with subauroral polarization streams (SAPS) at substorm time. *Journal of Geophysical Research: Space Physics*, 125, e2019JA027163. https://doi.org/10.1029/2019JA027163
- Zhang, S.-R., Erickson, P. J., Zhang, Y., Wang, W., Huang, C., Coster, A. J., et al. (2017). Observations of ion-neutral coupling associated with strong electrodynamic disturbances during the 2015 St. Patrick's Day storm. *Journal of Geophysical Research: Space Physics*, 122, 1314–1337. https://doi.org/10.1002/2016JA023307
- Zheng, Y., Brandt, P. C., Lui, A. T. Y., & Fok, M.-C. (2008). On ionospheric trough conductance and subauroral polarization streams: Simulation results. *Journal of Geophysical Research: Space Physics*, 113, A04209. https://doi.org/10.1029/2007JA012532
- Zou, S., Ridley, A., Jia, X., Boyd, E., Nicolls, M., Coster, A., et al. (2017). PFISR observation of intense ion upflow fluxes associated with an SED during the June 1, 2013 geomagnetic storm. *Journal of Geophysical Research: Space Physics*, 122, 2589–2604. https://doi.org/10.1002/2016JA023697

ZHANG ET AL. 16 of 16